APPLIED SCIENCES AND ENGINEERING

Minimized lithium trapping by isovalent isomorphism for high initial Coulombic efficiency of silicon anodes

Bin Zhu[1]*, **Guoliang Liu**[1]*, **Guangxin Lv**[1]*, **Yu Mu**[1], **Yunlei Zhao**[1], **Yuxi Wang**[1], **Xiuqiang Li**[1], **Pengcheng Yao**[1], **Yu Deng**[1]†, **Yi Cui**[2,3], **Jia Zhu**[1]†

Silicon demonstrates great potential as a next-generation lithium ion battery anode because of high capacity and elemental abundance. However, the issue of low initial Coulombic efficiency needs to be addressed to enable large-scale applications. There are mainly two mechanisms for this lithium loss in the first cycle: the formation of the solid electrolyte interphase and lithium trapping in the electrode. The former has been heavily investigated while the latter has been largely neglected. Here, through both theoretical calculation and experimental study, we demonstrate that by introducing Ge substitution in Si with fine compositional control, the energy barrier of lithium diffusion will be greatly reduced because of the lattice expansion. This effect of isovalent isomorphism significantly reduces the Li trapping by ~70% and improves the initial Coulombic efficiency to over 90%. We expect that various systems of battery materials can benefit from this mechanism for fine-tuning their electrochemical behaviors.

INTRODUCTION

Rechargeable lithium ion batteries (LIBs) at present are widely used as power supplies for portable electronics and electric vehicles (1–4). With conventional carbonaceous anodes approaching their theoretical capacity limits (5), silicon (Si) is emerging as a promising candidate for the next-generation LIB anode because of its high capacity (2, 6–8). Impressive progress has been made in the past decades through nanostructured designs (9–14), binder modification (15–17), and electrolyte development (18–20). However, the large irreversible capacity loss in the first cycle still remains an issue for commercialization. Typically, Si electrodes have the initial Coulombic efficiency (CE) of 70 to 85%, and those with larger specific area have a lower CE of 50 to 80% (21–29), far below that of commercial graphite anodes (~90 to 95%). Tremendous efforts have been made to address this issue (10, 11, 30–35). For example, Zhao et al. (31) proposed a prelithiation reagent with Li_xSi-Li_2O core-shell nanoparticles to compensate the initial capacity loss of a Si anode. Ko et al. (11) demonstrated Si nanolayer–embedded graphite as a hybrid anode to achieve high initial CE through avoiding surface side reactions. While Li loss due to the formation of the solid electrolyte interphase (SEI) has been heavily investigated in these previous works, Li trapping in the electrode, the other important mechanism for Li loss, has been rarely explored.

Recent study indicated that the effect of Li trapping in Si anodes accounts for approximately 30% of the initial Li loss for the first cycle (21) and leads to accelerated decay of Si anode capacity in the subsequent cycles (21, 36, 37). Thus, minimizing Li trapping is critical to improve the initial CE of Si anodes. Here, we introduce isovalent isomorphism into the development of alloy anodes by, for example, adding Ge atoms into a Si anode using a convenient ball milling method to increase Li migration and, therefore, to minimize Li trapping. Because of the minimized Li trapping, we effectively improve the initial CE of Si-based anode to over 90% (the highest reaches 94.1%). Through

careful theoretical calculation, Ge dopant atoms expand the lattice, which greatly reduces the energy barrier of Li diffusion, therefore minimizing Li trapping. This mechanism can also be applied and generalized for other atoms such as tin.

RESULTS AND DISCUSSION

Our own experiment through a careful study of inductively coupled plasma mass spectrometry (ICP-MS) (fig. S1) also confirms that a significant amount (about one-third) of the Li loss in the initial cycle is due to Li trapping in the Si anode. The mechanism behind this Li trapping can be illustrated by the diffusion modeling (21, 38, 39). During the lithiation of the Si anode, Li diffuses into the interior parts of the Si electrode until full lithiation to form $Li_{15}Si_4$ (fig. S1A). In the process of delithiation, as Li with limited capability of diffusion cannot diffuse out completely, some Li will be trapped in the Si electrode (fig. S1B).

Isovalent isomorphism, the increase of lattice constants because of partial substitution of a larger isovalent ion, has been previously used to achieve higher ionic conductivity of solid electrolytes (40–43). We first used a Ge isovalent ion to alloy with the Si anode. As shown in Fig. 1 (A and B), because of the partial replacement of Si by Ge, the lattice of the Li-Si-Ge phase is expanded compared to the original Li-Si phase, as illustrated in table S1. That generates two competing effects on Li atoms, depending on their positions relative to Ge atoms. For Li atoms far away from Ge, lattice expansion results in the larger local volumes occupied (the effect of "local expansion"). The lattice expansion causes the bond lengths (BLs) between Li and Si atom to increase. However, there is no change in the relative positions of Li and Si atoms. Thus, Li atoms can occupy larger local volumes to be helpful for Li diffusion in Li-Si anodes. For Li atoms close to Ge, such as those first neighbor atoms, the diffusion channels are narrowed because of the larger ionic radius of Ge (the "narrow channel" effect). Therefore, we surmise that as trace amounts of Ge atoms are added to replace Si, most of the Li atoms are far away from Ge atoms. The local expansion effect should dominate, which initially reduces the energy barrier of Li migration in the Si anode. If more Ge atoms are added in, then there would be more Li atoms sitting close to Ge atoms and the narrow channel effect is expected to dominate, which increases the energy barrier of Li migration.

[1]National Laboratory of Solid State Microstructures, College of Engineering and Applied Sciences, Jiangsu Key Laboratory of Artificial Functional Materials, Nanjing University, Nanjing 210093, P. R. China. [2]Department of Materials Science and Engineering, Stanford University, Stanford, CA, USA. [3]Stanford Institute for Materials and Energy Sciences, SLAC National Accelerator Laboratory, Menlo Park, CA, USA.
*These authors contributed equally to this work.
†Corresponding author. Email: jiazhu@nju.edu.cn (J.Z.); dengyu@nju.edu.cn (Y.D.)
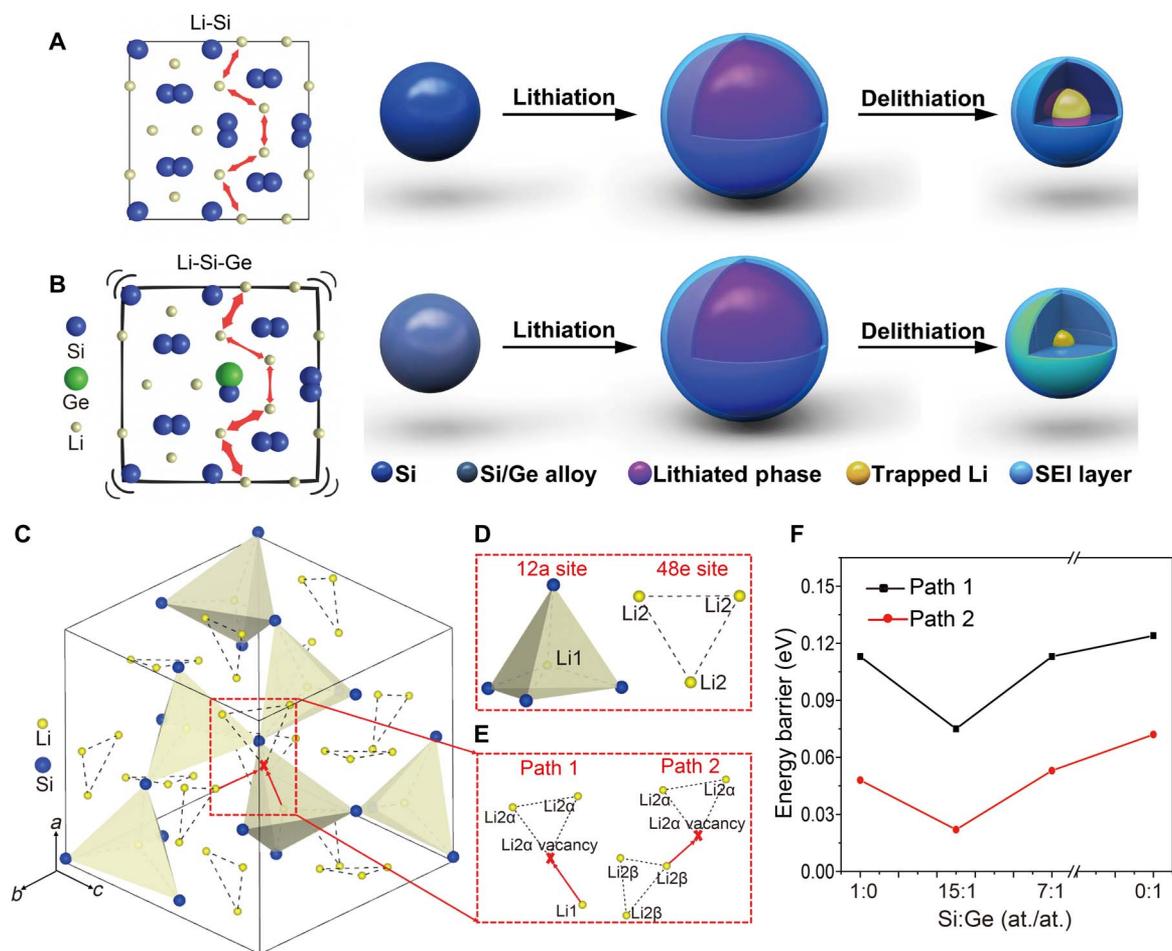
Fig. 1. Density functional theory calculations of energy barriers of Li diffusion in Li-Si-Ge. (**A**) Schematic of Li diffusion and lithiation/delithiation process in a Li-Si anode. (**B**) Schematic of Li diffusion and lithiation/delithiation process in a Li-Si-Ge anode. (**C**) Schematic unit cell of $Li_{15}Si_4$ alloy, in which Si and Li atoms are represented by blue and yellow balls, respectively. (**D**) Two types of Li atoms in $Li_{15}Si_4$ alloy. The Li1 atoms at 12a sites have the same distances from the four nearest Si atoms and are located in the center of tetrahedrons composed of these Si atoms, while three adjacent Li2 atoms at 48e sites constitute an equilateral triangle. (**E**) Schematics of two sets of pathways for Li migration in $Li_{15}Si_4$. (**F**) Relationships between energy barriers of Li migration along two pathways versus atomic ratios of Si to Ge in Li-Si-Ge.

Hence, we hypothesize that there exists an optimum atomic ratio of Si-Ge for minimized energy barrier and Li trapping.

To verify this mechanism, we first performed density functional theory (DFT) calculations to examine the energy barriers of Li diffusion in $Li_{15}Si_{4-x}Ge_x$ ($x = 0$, 0.25, 0.5, and 4.0) alloys. It was demonstrated in a previous study (*44*) that Li ions typically diffuse along two pathways: the Li2α vacancy defect moves to Li1 as Path 1 and the Li2α vacancy defect moves to Li2β in adjacent groups as Path 2 (Fig. 1E; see more details in Materials and Methods). As shown in Fig. 1F, when the amount of Ge is small, as in the case of $Li_{15}Si_{3.75}Ge_{0.25}$ (atomic ratio of Si:Ge, 15:1), the effect of local expansion dominates Li diffusion; therefore, Li atoms have smaller energy barriers of diffusion. The energy barriers of Li diffusion in $Li_{15}Si_{3.75}Ge_{0.25}$ (atomic ratio of Si:Ge, 15:1) along these two pathways decrease by 33.6% (from 0.113 to 0.075 eV for Path 1) and 54.2% (from 0.048 to 0.022 eV for Path 2), respectively. However, as the composition of Ge increases, as in the case of $Li_{15}Si_{3.5}Ge_{0.5}$ (atomic ratio of Si:Ge, 7:1), the narrow channel effect plays a dominant role; thus, the energy barriers of Li diffusion along Path 1 and Path 2 increase sharply to 0.124 and 0.072 eV, respectively. This can also be verified by the increase of binding force on each Li atom with Ge content, as

illustrated in table S1 and fig. S2. Therefore, DFT calculations clearly indicate that Li diffusion in Li-Si-Ge is dominated by the two competing effects of local expansion and narrow channel: a small amount of Ge alloyed into Si (atomic ratio of Si:Ge, 15:1) can lower the energy barriers of Li migration and reduce Li trapping.

To experimentally finely control the atomic ratio of Si to Ge, we prepared Si-Ge alloy particles with various atomic ratios ($Si_{15}Ge$ in Fig. 2A; other ratios are in fig. S4) by a convenient ball milling process (see more details in Materials and Methods). Si particles with a diameter of 150 nm were chosen to avoid self-pulverization, which is consistent with previous studies (*45*, *46*). A transmission electron microscope (TEM) image of $Si_{15}Ge$ particles and the diffraction pattern (Fig. 2B) confirm that the obtained $Si_{15}Ge$ particles are crystalline (inset of Fig. 2B) with a diameter around 150 nm. It is seen from the high-resolution TEM micrograph of the selected area in the $Si_{15}Ge$ particle that atomic lattice planes are separated by 3.13 Å, slightly larger than that of Si (3.10 Å) (Fig. 2C) (*47*). Images of scanning TEM (STEM) and corresponding energy-dispersive x-ray (EDX) spectroscopy elemental mapping reveal a uniform atomic scale mixing (Fig. 2D) of Si and Ge of $Si_{15}Ge$ particles. Scanning electron microscope (SEM) EDX
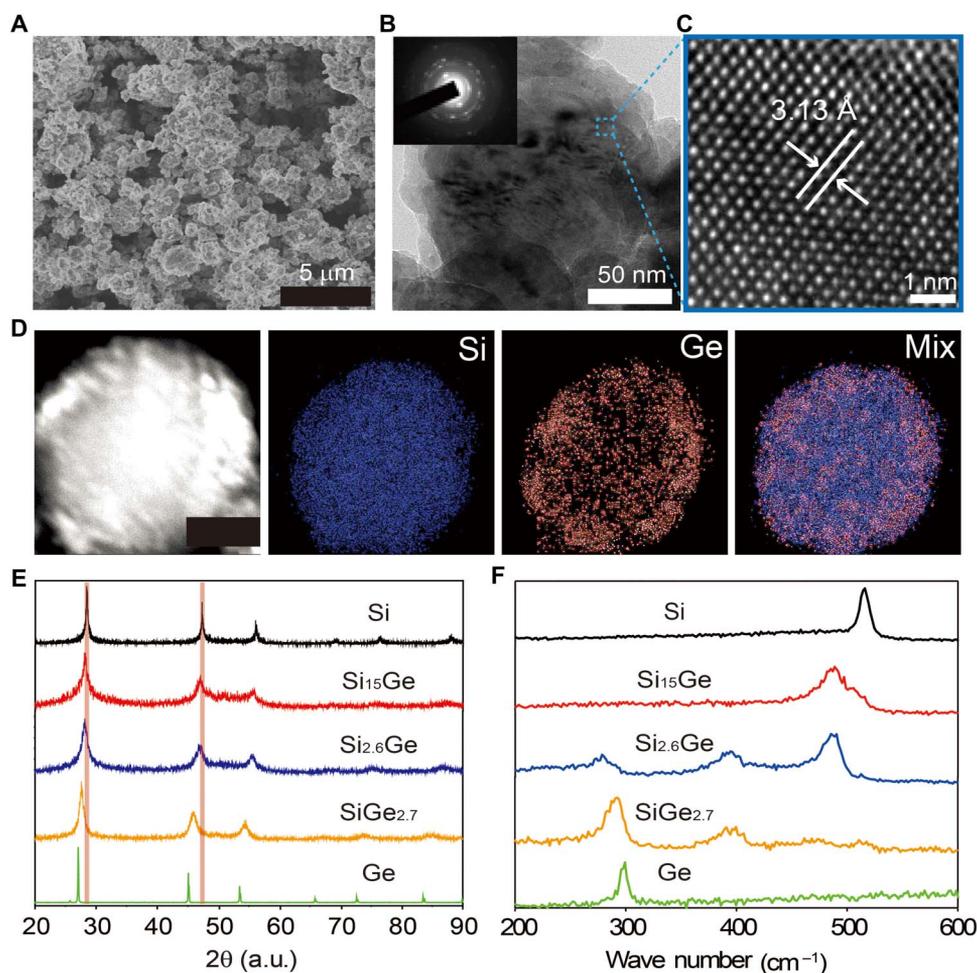
Fig. 2. Characterizations of the obtained Si-Ge alloy nanoparticles. (**A**) SEM and (**B**) TEM image of $Si_{15}Ge$ nanoparticles (inset: diffraction pattern). (**C**) High-resolution TEM of the selected part in (B). (**D**) STEM and corresponding EDX mapping images of Si and Ge (scale bar, 50 nm). (**E**) X-ray diffraction and (**F**) Raman results of various ratios of Si-Ge alloy nanoparticles. a.u., arbitrary units.

results confirm the precise atomic ratios of the obtained particles (fig. S4). The lattice expansion of Si-Ge alloy with more Ge is verified by a clear peak shift to smaller angles in x-ray diffraction (Fig. 2E) (48, 49). The Si-Si peak also shifts to lower wave numbers as the Ge content increases in Raman spectra (Fig. 2F), confirming that Ge atoms disrupted the Si lattice to form the Si-Ge alloy. These results together suggest that Si-Ge alloy particles with various atomic ratios of Si to Ge have been successfully prepared through ball milling.

To examine the electrochemical performance of Si-Ge alloy electrodes, half-cell measurements were first carried out using Li metal as a counter/reference electrode. For comparing CE, the thickness of each electrode was controlled to be around 10 μm. Figure 3A presents the typical cyclic voltammetry (CV) results of different Ge concentrations alloyed with Si in the first and second cycle at a scanning rate of 0.1 mV/s between 0 and 1 V versus Li/Li^+. In the CV of Si, a sharp redox peak below 0.1 V appears during the first Li insertion process, indicating the initial lithiation of crystalline Si. Along with the increase of Ge concentration, the redox peak shifts to a higher voltage, which is consistent with the Si-Ge alloy anode reported before (49). The discharge/charge profiles at the same current density of 0.1 C of these electrodes exhibit the precise lithiation platforms, clearly elucidating the differences of Ge addition in the Si anodes (Fig. 3B). It is observed

that the $Si_{15}Ge$ alloy anode delivered a charge and discharge capacity of 3200.8 and 3010.9 mA·hour/g at the initial cycle, corresponding to a high initial CE of 94.1% (Fig. 3B), which is higher than that of pure Si and other Si-Ge alloy electrodes, comparable to that of commercial graphite anodes. To avoid the interference, we measured 10 samples for each electrode at the same rate of 0.1 C and obtained the statistical results, as shown in Fig. 3C. It is obvious that the $Si_{15}Ge$ alloy electrodes exhibit higher initial CE ranging from 89.4 to 94.1% as compared with that of other Si-Ge alloy electrodes, which are almost always below 80% (21–29). Figure 3D lists the value of initial CE from this work, in comparison with other strategies reported previously such as electrolyte additives, structure design, and prelithiation. We also prepared new samples of each electrode for long cycles. Note that in the subsequent cycles, a $Si_{15}Ge$ electrode still maintains higher CE than other electrodes, which reaches up to 99% after only the third cycle (fig. S5B). It illustrates that isovalent isomorphism can minimize lithium trapping in each lithiation/delithiation cycle. Moreover, the various Si-Ge alloy anodes show a difference in terms of capacity retention (fig. S5A). With the increase of Ge concentration, the electrodes present more stable cycles (such as $Si_{2.6}Ge$, $SiGe_{2.7}$, and Ge) due to the higher intrinsic electronic/ionic conductivity, which is similar with that reported previously (48). For SiGe anodes with high
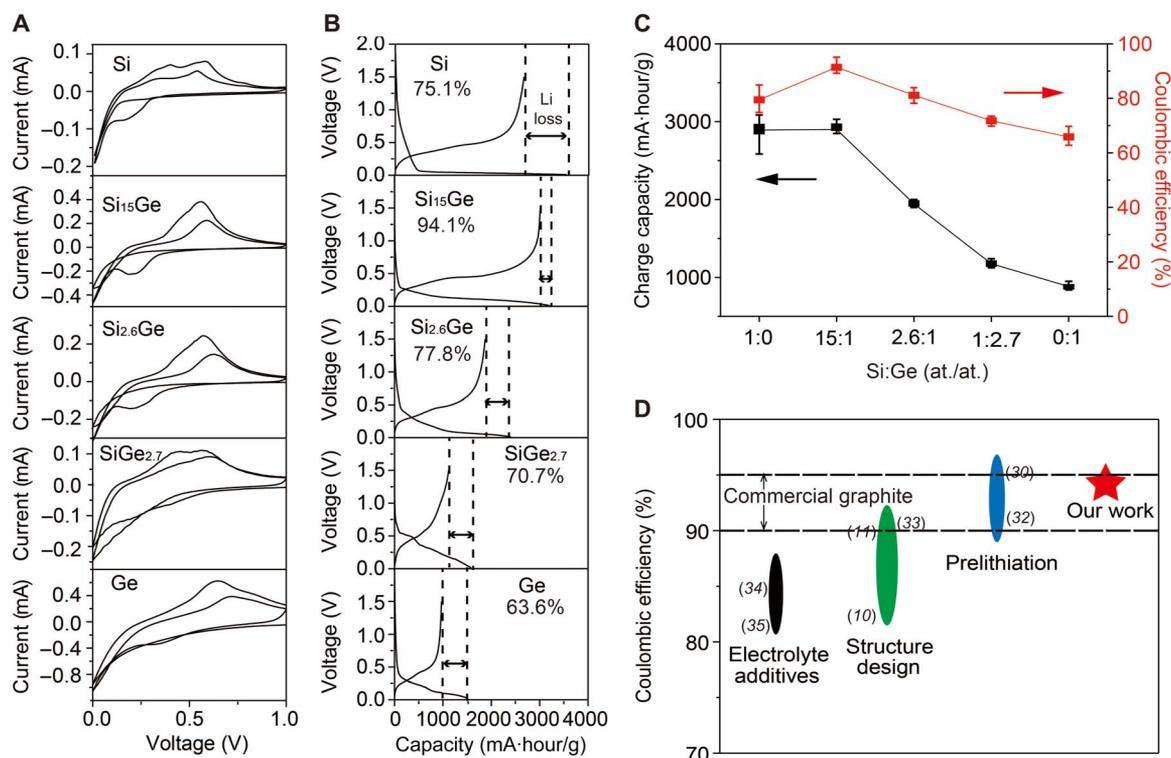
Fig. 3. Electrochemical performance of Si-Ge anodes with different atomic ratios. (**A**) CV curves of Si-Ge alloy electrodes with various atomic ratios. (**B**) Corresponding initial voltage profiles at the current density of 0.1 C, respectively. (**C**) Statistical results of initial charge capacities and CE of Si-Ge electrodes with various atomic ratios from 10 samples at the same rate of 0.1 C. (**D**) Initial CE values of our work and other strategies reported before.

Si composition as in the case of Si and $Si_{15}Ge$, they exhibit obvious capacity decay after 100 cycles, while their initial capacities are higher than that of other Si-Ge alloy anodes. It has been proved that structure design such as carbon coating can be effective to improve the long cycle stability of $Si_{15}Ge$ anodes (fig. S5C).

It is critical to figure out the exact cause of high initial CE of $Si_{15}Ge$ electrodes. Besides the formation of SEI and some Li trapped in the electrodes, the unstable structure due to volumetric change can also cause the first irreversible Li consumption in Si electrode. The volume expansion of Si-Ge alloy electrodes was unveiled by the SEM (Fig. 4, A and B, and fig. S6). The top-view images of Si and $Si_{15}Ge$ electrodes portray similar results. Both electrodes were maintained coalesced and intact; no pulverization or cracks were observed because of the small size of nanoparticles (<150 nm). The cross-sectional images reveal that the electrodes of Si and $Si_{15}Ge$ have similar thickness at pristine states (10.1 and 11.2 μm, respectively). For both of these two electrodes, thickness remains unchanged (10.8 and 11.4 μm, respectively) after the initial cycle, reflecting the cycle stability of electrodes. Therefore, it is safe to conclude that the initial Li loss due to pulverization induced by volume expansion should be negligible.

To identify the influence of SEI formation, we performed a TEM study of Si-Ge alloy electrodes after the initial cycle. The obvious evidence comes from TEM images of the cycled Si and $Si_{15}Ge$, whose surfaces are found to be covered with an approximately 10-nm-thick SEI layer (Fig. 4, C and D), when compared with the pristine state. Other Si-Ge alloy particles with different atomic ratios present similar SEI thickness after the first cycle, while Ge particles exhibit a thicker SEI layer (fig. S7). X-ray photoelectron spectroscopy was exploited to char-

acterize the SEI components of Si and $Si_{15}Ge$, suggesting the same SEI components for Si and $Si_{15}Ge$ (Fig. 4E).

To further study the growth kinetics and Li ion/electron transport of SEI films, electrochemistry impedance spectroscopy (EIS) was carried out. The electrochemical impedances of all cells based on Si-Ge electrodes with various atomic ratios were measured after the first cycle. Figure 4F presents the EIS of Si and $Si_{15}Ge$ after the first charge to 1.5 V. It is clear that both curves are composed of two high-frequency suppressed semicircles and a sloping line in the low-frequency region, which correspond to the SEI film formation, the charge-transfer reaction, and the Li^+ diffusion effect on the electrode-electrolyte interfaces, respectively. On the basis of the equivalent circuit model (inset of Fig. 4F), the R_{SEI} (SEI film resistance) of a $Si_{15}Ge$ cell is about 128.2 ohms, which approximates to 123.1 ohms of the Si cell's R_{SEI}. It is consistent with the TEM results (Fig. 4, C and D) that SEI with a similar thickness was formed during electrochemical cycling for Si and $Si_{15}Ge$. The SEI impedances of other Si-Ge alloy cells were fairly similar (around 150 ohms), while that of the Ge cell showed a higher value of 175 ohms (fig. S8). In general, it seems that, from the statistical results of R_{SEI} and SEI thickness, no distinct differences are shown in the formed SEI for five different samples of Si-Ge electrodes with different atomic ratios (Fig. 4G).

To understand the origin of the increase of initial CE for the $Si_{15}Ge$ electrode, we exploited ICP-MS to determine the Li contents of different Si-Ge alloy electrodes after the first cycle (seen in Materials and Methods). It was found that $Si_{15}Ge$ electrodes have much less amounts of trapped Li (0.9 to 1.2%) compared to other electrodes (4.6 to 11.1%). For clarity, we define a value (η) to represent the concentration of
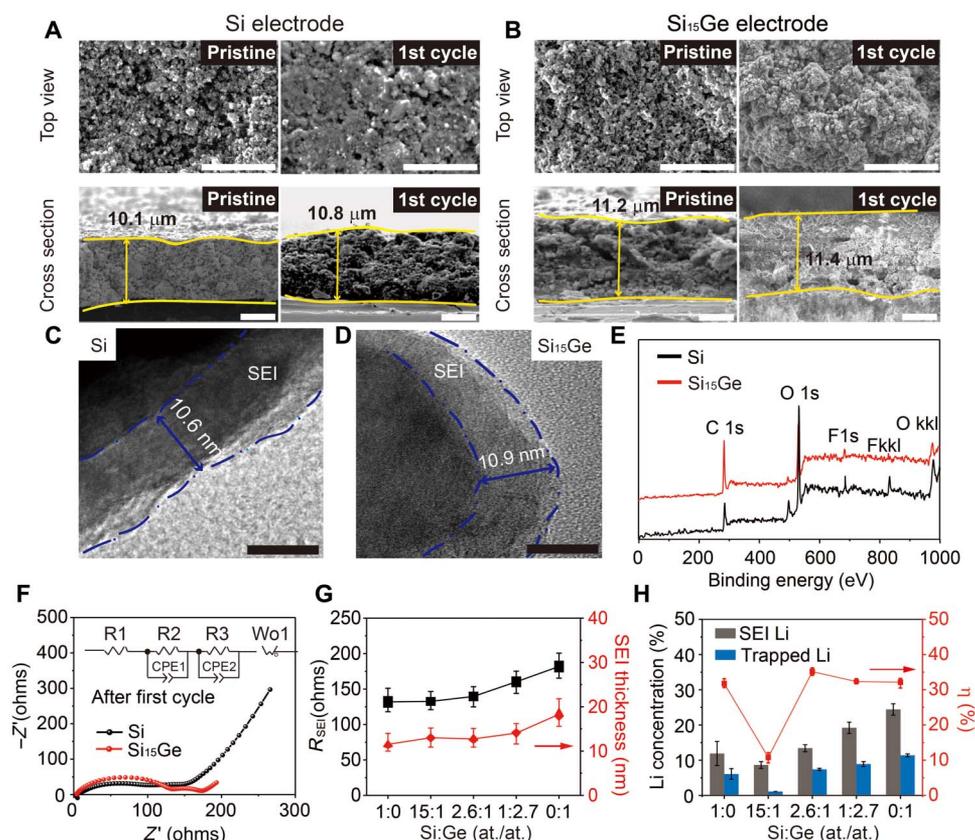
Fig. 4. Characterizations of Si-Ge alloy anodes before/after initial cycle. (**A**) Top view and cross section of Si electrode and (**B**) $Si_{15}Ge$ electrode before and after initial cycle [scale bars, 10 μm (top view) and 5 μm (cross section)]. (**C**) TEM of Si and (**D**) $Si_{15}Ge$ nanoparticle after initial cycle (scale bar, 10 nm). (**E**) X-ray photoelectron spectroscopy results of Si and $Si_{15}Ge$ electrodes after initial cycle. (**F**) Electrochemistry impedance spectroscopy (EIS) result of Si and $Si_{15}Ge$ after initial cycle. (**G**) The statistical results of R_{SEI} and SEI thickness from five different samples. (**H**) Li_{SEI} and trapped Li from ICP results and η value.

trapped Li in the initial entire Li loss (η = trapped Li/Li loss and Li loss = SEI Li + trapped Li). It is interesting to find that the η of $Si_{15}Ge$ electrodes was 9.2 to 11.1%, far lower than that of other electrodes (~30%), suggesting minimized Li trapping in the $Si_{15}Ge$ electrode, which is consistent with the DFT calculation (Fig. 1F). It is also noted that, although the thickness of SEI for Si and $Si_{15}Ge$ is similar (Fig. 4G), the concentration of Li from the SEI (Li_{SEI}) also reduced from ~8.5 to 15.3% (Si) to ~7.7 to 9.5%. This reduced Li_{SEI} in a $Si_{15}Ge$ anode may be attributed to improved Li kinetics because of lower energy barriers of Li migration, consequently resulting in the formation of SEI with low density (50–53).

To examine whether this mechanism of isovalent isomorphism can be applied to other isovalent atoms, we also performed the same study for Si-Sn alloys. The energy barriers of Li migration along two pathways in Li-Si-Sn alloys were calculated (see more details in tables S3 and S4), which show a similar trend as that in Li-Si-Ge alloys (fig. S2 and Fig. 1F). We also prepared Si-Sn alloy particles with various atomic ratios as anodes to examine the electrochemical performance. As shown in fig. S9, the Si-Sn alloy with small percentage of Sn ($Si_{18.2}Sn$) shows the highest initial CE reaching 93.6%. According to ICP results (table S5), the η value of $Si_{18.2}Sn$ is 12.03%, the lowest among all the Si-Sn alloys, consistent with the calculation result (fig. S3B). Therefore, our proposed mechanism is generalized for isovalent atoms to minimize Li trapping.

In summary, we demonstrated that through a fine compositional control of alloy anodes, isovalent isomorphism can be used to effectively

reduce the energy barriers of Li diffusion and therefore reduce Li trapping and increase initial CE. As an example, anodes based on a Si-Ge alloy (atomic ratio of Si:Ge, 15:1) have significant reduced Li trapping (70% decrease compared to Si) and high initial CE reaching 94.1%. This practical approach can be applied to other isovalent atoms (such as tin) and complementary to other structural designs and engineering methods. Therefore, this effect based on isovalent isomorphism provides an extra knob for fine-tuning electrochemical Li behaviors in various material systems.

MATERIALS AND METHODS
Computational methods
It is known that the $Li_{15}Si_{4-x}Ge_x$ phase is in the fully lithiated state at room temperature, in which all the Si (and Ge) atoms at 16c sites are surrounded by Li atoms while Li atoms are classified into two groups according to the symmetry: Li1 atoms at 12a sites and Li2 atoms at 48e sites (Fig. 1, C and D). To theoretically find out the stable structures of $Li_{15}Si_{4-x}Ge_x$ (x = 0, 0.25, 0.5, and 4.0) alloys, their structure optimizations were first performed in the frame of DFT with the program package CASTEP (54, 55), using the plane-wave (PW) ultrasoft pseudopotential method and the Perdew-Wang (PW91) form of generalized gradient approximation (GGA) exchange-correlation energy functional (56). To quantificationally estimate the covalent interactions on each Li atom in $Li_{15}Si_{4-x}Ge_x$, the average bond orders (BO) and BLs were calculated

by using a projection of PW states onto a molecular orbital basis in the Mulliken population analysis (57).

Then, depending on the type of Li atoms and the distances between them, we chose two sets of pathways for Li migration in $Li_{15}Si_{4-x}Ge_x$ to examine the energy barriers by performing transition state (TS) searches. As seen in Fig. 1E, for the first set of pathways (Path 1), the Li2α vacancy defect moves to Li1, while for the second set of pathway (Path 2), Li2α vacancy defect migrates to Li2β in adjacent groups. The TS searches of Li migration in $Li_{15}Si_{4-x}Ge_x$ were carried out using the program package DMol3 (58, 59) with double numerical with polarization basis sets and the complete linear synchronous transit/quadratic synchronous transit method (60).

Preparation of particles
The particles with a diameter of ~150 nm were prepared by ball milling. After mixing the silicon powder (99.9%; Alfa Aesar) and germanium (99.99%; Alfa Assar), the mixture was ball-milled with a rotation speed of 750 rpm. Before fabricating electrodes, the obtained particles were etched by 5% HF for 5 min to avoid oxidation.

Preparation of the electrodes
The control electrode was prepared by dissolving the mixture of 60 mg of nanoparticles, 20 mg of carbon black, and 20 mg of sodium carboxymethyl cellulose binder in deionized water (0.6 ml) to make slurry. After stirring, the slurry was cast onto a copper foil and then dried in a vacuum oven at 110°C.

Half cells for testing
Coin-type cells (2032) were fabricated inside an Ar-filled glove box using a Celgard 2250 separator. A Si-Ge alloy electrode and Li metal foil were prepared as two electrodes. The electrolyte used was 1.0 M $LiPF_6$ in 1:1 v/v ethylene carbonate/diethyl carbonate with 2 weight % vinylene carbonate (Guotai Huarong) added to improve the cycling stability. The electrochemical tests were performed using a LANHE CT2001A for cycling performance and electrochemical workstation for typical CV. If without special instructions, then the rate used for cycling test was 0.1 C.

SEM and TEM
The nanoparticle samples were prepared by casting the nanoparticles on the copper colloids and observed by SEM (TESCAN MIRA3). The electrode samples were prepared by sticking the electrodes to the copper colloids directly. The electrode after cycling was treated with acetonitrile to remove the electrolyte in the Ar-filled glove box before producing the SEM samples. Then, the front and cross section of the electrodes were also observed by SEM. The nanoparticle TEM samples were prepared by dissolving the nanoparticles in alcohol and stirring the mixture for 10 min. Then, the mixture was cast on the copper grid and dried in the air. The electrode samples were prepared by mixing the dried acetonitrile-treated electrode and alcohol. The mixture was stirred for 1 hour, and the liquid with deciduous electrode particles was cast on the copper grid. Then, the sample was dried in the air. Both samples of nanoparticles were observed by TEM (TitanX, FEI, super EDX, 200 kV).

ICP–atomic emission spectroscopy test
The electrode after 1 cycle was treated with acetonitrile to remove the electrolyte and dried in the Ar-filled glove box. Then, the electrodes were dissolved in 5 ml of deionized water overnight to completely remove the extra Li on the electrode. Then, the electrodes were treated in 0.5 M HCl to dissolve SEI; supernatants (1 ml) were extracted from the solution and were tested using an ICP-AES (atomic emission spectroscopy) instrument to get the Li^+ concentration of SEI. After washing the remained electrodes with ultrapure water, 10% HCl, 20% HNO_3, and 8% HF were added to dissolve Si, Ge, and the trapped Li. After centrifugation, 1 ml of solution from supernatants was tested using an ICP-AES instrument to determine the trapped Li. Last, the amount of trapped Li was calculated.

REFERENCES AND NOTES
1. D. Larcher, J.-M. Tarascon, Towards greener and more sustainable batteries for electrical energy storage. *Nat. Chem.* **7**, 19–29 (2015).
2. Y. Sun, N. Liu, Y. Cui, Promises and challenges of nanomaterials for lithium-based rechargeable batteries. *Nat. Energy* **1**, 16071 (2016).
3. M. Armand, J.-M. Tarascon, Building better batteries. *Nature* **451**, 652–657 (2008).
4. P.-G. Bruce, S. A. Freunberger, L. J. Hardwick, J.-M. Tarascon, Li–O$_2$ and Li–S batteries with high energy storage. *Nat. Mater.* **11**, 19–29 (2012).
5. P. Poizot, S. Laruelle, S. Grugeon, L. Dupont, J.-M. Tarascon, Nano-sizedtransition-metaloxidesas negative-electrode materials for lithium-ion batteries. *Nature* **407**, 496–499 (2000).
6. Y. Sun, H.-W. Lee, Z.-W. Seh, N. Liu, J. Sun, Y. Li, Y. Cui, High-capacity battery cathode prelithiation to offset initial lithium loss. *Nat. Energy* **1**, 15008 (2016).
7. J. W. Choi, D. Aurbach, Promise and reality of post-lithium-ion batteries with high energy densities. *Nat. Rev. Mater.* **1**, 16013 (2016).
8. M. N. Obrovaca, L. Christensena, D. B. Lea, J. R. Dahn, Alloy design for lithium-ion battery anodes. *J. Electrochem. Soc.* **154**, 849–855 (2007).
9. A. Magasinski, P. Dixon, B. Hertzberg, A. Kvit, J. Ayala, G. Yushin, High-performance lithium-ion anodes using a hierarchical bottom-up approach. *Nat. Mater.* **9**, 353–358 (2010).
10. N. Liu, Z. Lu, J. Zhao, M. T. McDowell, H.-W. Lee, W. Zhao, Y. Cui, A pomegranate-inspired nanoscale design for large-volume-change lithium battery anodes. *Nat. Nanotechnol.* **9**, 187–192 (2014).
11. M. Ko, S. Chae, J. Ma, N. Kim, H.-W. Lee, Y. Cui, J. Cho, Scalable synthesis of silicon-nanolayer-embedded graphite for high-energy lithium-ion batteries. *Nat. Energy* **1**, 16113 (2016).

12. C. K. Chan, H. Peng, G. Liu, K. McIlwrath, X. Zhang, R. A. Huggins, Y. Cui, High-performance lithium battery anodes using silicon nanowires. *Nat. Nanotechnol.* **3**, 31–35 (2008).

13. X. L. Li, M. Gu, S. Y. Hu, R. Kennard, P. F. Yan, X. L. Chen, C. M. Wang, M. J. Sailor, J. G. Zhang, J. Liu, Mesoporous silicon sponge as an anti-pulverization structure for high-performance lithium ion battery anodes. *Nat. Commun.* **5**, 4105 (2014).

14. M.-H. Park, M. G. Kim, J. Joo, K. Kim, J. Kim, S. Ahn, Y. Cui, J. Cho, Silicon nanotube battery anodes. *Nano Lett.* **9**, 3844–3847 (2009).

15. S. Choi, T.-w. Kwon, A. Coskun, J. W. Choi, Highly elastic binders integrating polyrotaxanes for silicon microparticle anodes in lithium ion batteries. *Science* **357**, 279–283 (2017).

16. J. Li, R. B. Lewis, J. R. Dahn, Sodium carboxymethyl cellulose: A potential binder for Si negative electrodes for Li-ion batteries. *Electrochem. Solid St.* **10**, 17–20 (2006).

17. I. Kovalenko, B. Zdyrko, A. Magasinski, B. Hertzberg, Z. Milicev, R. Burtovyy, I. Luzinov, G. Yushin, A major constituent of brown algae for use in high-capacity Li-ion batteries. *Science* **334**, 75–79 (2011).

18. V. Etacheri, O. Haik, Y. Goffer, G. A. Roberts, I. C. Stefan, R. Fasching, D. Aurbach, Effect of fluoroethylene carbonate (FEC) on the performance and surface chemistry of Si-nanowire Li-ion battery anodes. *Langmuir* **28**, 965–976 (2012).

19. L. B. Chen, K. Wang, X. H. Xie, J. Xie, Effect of vinylene carbonate (VC) as electrolyte additive on electrochemical performance of Si film anode for lithium ion batteries. *J. Power Sources* **174**, 538–543 (2007).

20. Y.-M. Lin, K. C. Klavetter, P. R. Abel, N. C. Davy, J. L. Snider, A. Heller, C. B. Mullins, High performance silicon nanoparticle anode in fluoroethylene carbonate-based electrolyte for Li-ion batteries. *Chem. Commun.* **48**, 7268–7270 (2012).

21. D. Rehnlund, F. Lindgren, S. Böhme, T. Nordh, Y. M. Zou, J. Pettersson, U. Bexell, M. Boman, K. Edström, L. Nyholm, Lithium trapping in alloy forming electrodes and current collectors for lithium based batteries. *Energ. Environ. Sci.* **10**, 1350–1357 (2017).

22. M. Y. Ge, J. P. Rong, X. Fang, C. W. Zhou, Porous doped silicon nanowires for lithium ion battery anode with long cycle life. *Nano Lett.* **12**, 2318–2323 (2012).

23. H. Wu, G. Chan, J. W. Choi, I. Ryu, Y. Yao, M. T. McDowell, S. W. Lee, A. Jackson, Y. Yang, L. B. Hu, Y. Cui, Stable cycling of double-walled silicon nanotube battery anodes through solid–electrolyte interphase control. *Nat. Nanotechnol.* **7**, 310–315 (2012).

24. I. H. Son, J. H. Park, S. Kwon, S. Park, M. H. Rümmeli, A. Bachmatiuk, H. J. Song, J. Ku, J. W. Choi, J.-M. Choi, S.-G. Doo, H. Chang, Silicon carbide-free graphene growth on silicon for lithium-ion battery with high volumetric energy density. *Nat. Commun.* **6**, 7393 (2015).

25. Z. Lu, N. Liu, H.-W. Lee, J. Zhao, W. Li, Y. Li, Y. Cui, Nonfilling carbon coating of porous silicon micrometer-sized particles for high-performance lithium battery anodes. *ACS Nano* **9**, 2540–2547 (2015).

26. C. F. Shen, X. Fang, M. Y. Ge, A. Y. Zhang, Y. H. Liu, Y. Q. Ma, M. Mecklenburg, X. Nie, C. W. Zhou, Hierarchical carbon-coated ball-milled silicon: Synthesis and applications in free-standing electrodes and high-voltage full lithium-ion batteries. *ACS Nano* **12**, 6280–6291 (2018).

27. S. Q. Chen, L. F. Shen, P. A. van Aken, J. Maier, Y. Yu, Dual-functionalized double carbon shells coated silicon nanoparticles for high performance lithium-ion batteries. *Adv. Mater.* **29**, 1605650 (2017).

28. H. J. Tian, X. J. Tan, F. X. Xin, C. S. Wang, W. Q. Han, Micro-sized nano-porous Si/C anodes for lithium ion batteries. *Nano Energy* **11**, 490–499 (2015).

29. T. Yoon, T. Bok, C. Kim, Y. Na, S. Park, K. S. Kim, Mesoporous silicon hollow nanocubes derived from metal–organic framework template for advanced lithium-ion battery anode. *ACS Nano* **11**, 4808–4815 (2017).

30. J. Zhao, Z. D. Lu, H. T. Wang, W. Liu, H.-W. Lee, K. Yan, D. Zhuo, D. C. Lin, N. Liu, Y. Cui, Artificial solid electrolyte interphase-protected lixsi nanoparticles: An efficient and stable prelithiation reagent for lithium-ion batteries. *J. Am. Chem. Soc.* **137**, 8372–8375 (2015).

31. J. Zhao, Z. D. Lu, N. Liu, H.-W. Lee, M. T. McDowell, Y. Cui, Dry-air-stable lithium silicide-lithium oxide core-shell nanoparticles as high-capacity prelithiation reagents. *Nat. Commun.* **5**, 5088 (2014).

32. H. J. Kim, S. Choi, S. J. Lee, M. W. Seo, J. G. Lee, E. Deniz, Y. J. Lee, E. K. Kim, J. W. Choi, Controlled prelithiation of silicon monoxide for high performance lithium-ion rechargeable full cells. *Nano Lett.* **16**, 282–288 (2016).

33. Y. Li, K. Yan, H.-W. Lee, Z. D. Lu, N. Liu, Y. Cui, Growth of conformal graphene cages on micrometre-sized silicon particles as stable battery anodes. *Nat. Energy* **1**, 15029 (2016).

34. C. Xu, F. Lindgren, B. Philippe, F. Björefors, K. Edström, T. Gustafsson, Improved performance of the silicon anode for li-ion batteries: Understanding the surface modification mechanism of fluoroethylene carbonate as an effective electrolyte additive. *Chem. Mater.* **27**, 2591–2599 (2015).

35. K. Schroder, J. Alvarado, T. A. Yersak, J. C. Li, N. Dudney, L. J. Webb, Y. S. Meng, K. J. Stevenson, The effect of fluoroethylene carbonate as an additive on the solid electrolyte interphase on silicon lithium-ion electrodes. *Chem. Mater.* **27**, 5531–5542 (2015).

36. A. L. Michan, G. Divitini, A. J. Pell, M. Leskes, C. Ducati, C. P. Grey, Solid electrolyte interphase growth and capacity loss in silicon electrodes. *J. Am. Chem. Soc.* **138**, 7918–7931 (2016).

37. K. Ogata, E. Salager, C. J. Kerr, A. E. Fraser, C. Ducati, A. J. Morris, S. Hofmann, C. P. Grey, Revealing lithium-silicide phase transformations in nano-structured silicon-based lithium ion batteries via in situ NMR spectroscopy. *Nat. Commun.* **5**, 3217 (2014).

38. G. Oltean, C.-W. Tai, K. Edström, L. Nyholm, On the origin of the capacity fading for aluminium negative electrodes in Li-ion batteries. *J. Power Sources* **269**, 266–273 (2014).

39. W. C. Maskell, J. R. Owen, Cycling behavior of thin film LiAl electrodes with liquid and solid electrolytes. *J. Electrochem. Soc.* **132**, 1602–1607 (1985).

40. S. H. Santagneli, H. V. A. Baldacim, S. J. L. Ribeiro, S. Kundu, A. C. M. Rodrigues, C. Doerenkamp, H. Eckert, Preparation, structural characterization, and electrical conductivity of highly ion-conducting glasses and glass ceramics in the system $Li_{1+x}Al_xSnGe_{2-(x+y)}(PO4)_3$. *J. Phys. Chem. C* **120**, 14556–14567 (2016).

41. Y. Sun, K. Suzuki, S. Hori, M. Hirayama, R. Kanno, Superionic conductors: $Li_{10+\delta}[Sn_ySi_{1-y}]_{1+\delta}P_{2-\delta}S_{12}$ with a $Li_{10}GeP_2S_{12}$-type structure in the Li_3PS_4–Li_4SnS_4–Li_4SiS_4 Quasi-ternary system. *Chem. Mater.* **29**, 5858–5864 (2017).

42. T. Krauskopf, S. P. Culver, W. G. Zeier, Bottleneck of diffusion and inductive effects in $Li_{10}Ge_{1-x}Sn_xP_2S_{12}$. *Chem. Mater.* **30**, 1791–1798 (2018).

43. Y. Kato, R. Saito, M. Sakano, A. Mitsui, M. Hirayama, R. Kanno, Synthesis, structure and lithium ionic conductivity of solid solutions of $Li_{10}(Ge_{1-x}M_x)P_2S_{12}$ (M = Si, Sn). *J. Power Sources* **271**, 60–64 (2014).

44. J. Moon, B. Lee, M. Cho, K. Cho, Ab initio and kinetic Monte Carlo study of lithium diffusion in LiSi, $Li_{12}Si_7$, $Li_{13}Si_5$ and $Li_{15}Si_4$. *J. Power Sources* **328**, 558–566 (2016).

45. B. Zhu, Y. Jin, Y. L. Tan, L. Q. Zong, Y. Hu, L. Chen, Y. B. Chen, Q. Zhang, J. Zhu, Scalable production of Si nanoparticles directly from low grade sources for lithium-ion battery anode. *Nano Lett.* **15**, 5750–5754 (2015).

46. X. Liu, L. Zhong, S. Huang, S. Mao, T. Zhu, J. Huang, Size-dependent fracture of silicon nanoparticles during lithiation. *ACS Nano* **6**, 1522–1531 (2012).

47. A. M. Morales, C. M. Lieber, A laser ablation method for the synthesis of crystalline semiconductor nanowires. *Science* **279**, 208–211 (1998).

48. P. R. Abel, A. M. Chockla, Y.-M. Lin, V. C. Holmberg, J. T. Harris, B. A. Korgel, A. Heller, C. B. Mullins, Nanostructured $Si_{(1-x)}Ge_x$ for tunable thin film lithium-ion battery anodes. *ACS Nano* **7**, 2249–2257 (2013).

49. H. Lee, J. Cho, $Sn_{78}Ge_{22}$@Carbon core–shell nanowires as fast and high-capacity lithium storage media. *Nano Lett.* **7**, 2638–2641 (2007).

50. E. Peled, D. Golodnitsky, G. Ardel, Advanced model for solid-electrolyte interphase electrodes in liquid and polymer electrolytes. *J. Electrochem. Soc.* **144**, L208–L210 (1997).

51. E. Peled, The electrochemical behavior of alkali and alkaline earth metals in nonaqueous battery systems—The solid electrolyte interphase model. *J. Electrochem. Soc.* **126**, 2047–2051 (1979).

52. D. Aurbach, Y. Ely, A. Zaban, The surface chemistry of lithium electrodes in alkyl carbonate solutions. *J. Electrochem. Soc.* **141**, L1–L3 (1994).

53. Y. Li, W. Huang, Y. Li, A. Pei, D. T. Boyle, Y. Cui, Correlating structure and function of battery interphases at atomic resolution using cryoelectron microscopy. *Joule* **2**, 2167–2177 (2018).

54. M. D. Segall, P. J. D. Lindan, M. J. Probert, C. J. Pickard, P. J. Hasnip, S. J. Clark, M. C. Payne, First-principles simulation: ideas, illustrations and the CASTEP code. *J. Phy. Condens. Mat.* **14**, 2717–2744 (2002).

55. S. J. Clark, M. D. Segall, C. J. Pickard, P. J. Hasnip, M. I. J. Probert, K. Refson, M. C. Payne, First principles methods using CASTEP. *Z. Kristallogr. Cryst. Mater.* **220**, 567–570 (2005).

56. J. P. Perdew, J. A. Chevary, S. H. Vosko, K. A. Jackson, M. R. Pederson, D. J. Singh, C. Fiolhais, Atoms, molecules, solids, and surfaces: Applications of the generalized gradient approximation for exchange and correlation. *Phys. Rev. B* **46**, 6671–6687 (1992).

57. R. S. Mulliken, Electronic population analysis on LCAO-MO molecular wave functions. I. *J. Chem. Phys.* **23**, 1833 (1955).

58. B. Delley, An all-electron numerical method for solving the local density functional for polyatomic molecules. *J. Chem. Phys.* **92**, 508–517 (1990).

59. B. Delley, From molecules to solids with the $DMol^3$ approach. *J. Chem. Phys.* **113**, 7756–7764 (2000).

60. T. A. Halgren, W. N. Lipscomb, The synchronous-transit method for determining reaction pathways and locating molecular transition states. *Chem. Phys. Lett.* **49**, 225–232 (1977).

Citation: B. Zhu, G. Liu, G. Lv, Y. Mu, Y. Zhao, Y. Wang, X. Li, P. Yao, Y. Deng, Y. Cui, J. Zhu, Minimized lithium trapping by isovalent isomorphism for high initial Coulombic efficiency of silicon anodes. *Sci. Adv.* **5**, eaax0651 (2019).

Science Advances

Minimized lithium trapping by isovalent isomorphism for high initial Coulombic efficiency of silicon anodes

Bin Zhu, Guoliang Liu, Guangxin Lv, Yu Mu, Yunlei Zhao, Yuxi Wang, Xiuqiang Li, Pengcheng Yao, Yu Deng, Yi Cui and Jia Zhu

ARTICLE TOOLS	http://advances.sciencemag.org/content/5/11/eaax0651
SUPPLEMENTARY MATERIALS	http://advances.sciencemag.org/content/suppl/2019/11/08/5.11.eaax0651.DC1
REFERENCES	This article cites 59 articles, 6 of which you can access for free http://advances.sciencemag.org/content/5/11/eaax0651#BIBL
PERMISSIONS	http://www.sciencemag.org/help/reprints-and-permissions

Use of this article is subject to the Terms of Service